Key Points:
- Wave-like Faraday rotation fluctuations were identified in the lower corona
- The wave energies scale as a power law in the 1-20 mHz frequency regime
- Faraday rotation fluctuation analysis enables tracking of modeled Alfven wave energy flux

Correspondence to:
D. B. Wexler,
dwexler@mit.edu

Faraday rotation fluctuations of MESSENGER radio signals through the equatorial lower corona near solar minimum

D. B. Wexler[1], E. A. Jensen[2], J. V. Hollweg[3], C. Heiles[4], A. I. Efimov[5], J. Vierinen[6,7], and A. J. Coster[2]

[1]Computational Engineering and Science Research Centre, University of Southern Queensland, Toowoomba, Australia, [2]Planetary Science Institute, Tucson, Arizona, [3]Department of Physics, University of New Hampshire, Durham, New Hampshire, [4]Department of Astronomy, University of California, Berkeley, Berkeley, California, [5]Kotel'nikov Institute of Radio Engineering and Electronics, Moscow, Russia, [6]Department of Physics and Technology, University of Tromsø, Tromsø, Norway, [7]MIT Haystack Observatory, Westford, Massachusetts

Abstract Faraday rotation (FR) of transcoronal radio transmissions from spacecraft near superior conjunction enables study of the temporal variations in coronal plasma density, velocity, and magnetic field. The MESSENGER spacecraft 8.4 GHz radio, transmitting through the corona with closest line-of-sight approach 1.63–1.89 solar radii and near-equatorial heliolatitudes, was recorded soon after the deep solar minimum of solar cycle 23. During egress from superior conjunction, FR gradually decreased, and an overlay of wave-like FR fluctuations (FRFs) with periods of hundreds to thousands of seconds was found. The FRF power spectrum was characterized by a power law relation, with the baseline spectral index being -2.64. A transient power increase showed relative flattening of the spectrum and bands of enhanced spectral power at 3.3 mHz and 6.1 mHz. Our results confirm the presence of coronal FRF similar to those described previously at greater solar offset. Interpreted as Alfvén waves crossing the line of sight radially near the proximate point, low-frequency FRF convey an energy flux density higher than that of the background solar wind kinetic energy, but only a fraction of that required to accelerate the solar wind. Even so, this fraction is quite variable and potentially escalates to energetically significant values with relatively modest changes in estimated magnetic field strength and electron concentration. Given the uncertainties in these key parameters, as well as in solar wind properties close to the Sun at low heliolatitudes, we cannot yet confidently assign the quantitative role for Alfvén wave energy from this region in driving the slow solar wind.

1. Introduction

The plasma surrounding the Sun exhibits wave-like magnetohydrodynamic (MHD) fluctuations over a wide range of temporal-spatial scales and heliocentric distances [*Ofman*, 2010; *Nakariakov and Verwichte*, 2005; *Arregui*, 2015; *Mathioudakis et al.*, 2013]. Despite much investigation, the role these waves play in solar wind acceleration and coronal energy transfer remains unknown. An improved understanding of coronal disturbances and their MHD wave signatures is necessary to more fully understand space weather origins and achieve early detection of adverse geo-effective events.

Coronal dynamics can be studied in extreme ultraviolet (EUV) space telescope imaging from the solar surface out to about 1.35 solar radii ($R_\odot$, heliocentric). A great wealth of information has been obtained on coronal structure and oscillatory phenomena at this close solar range [*Arregui*, 2015]. Beyond this distance, and in dark open-field regions of the near-corona, Faraday rotation (FR) of linearly polarized transcoronal signals currently provides one of the few means to probe the corona for magnetic field information [*Hollweg*, 2008; *Bird*, 2007; *Jensen*, 2007; *Mancuso and Spangler*, 2000]. Coronal sounding using FR has been accomplished by using both natural radio sources [*Kooi et al.*, 2014; *Mancuso and Spangler*, 1999; *You et al.*, 2012] and spacecraft transmissions [e.g., *Efimov et al.*, 2000, 1993; *Chashei et al.*, 2000; *Bird*, 2007; *Jensen et al.*, 2005, 2013a]. The majority of these FR studies provided information for coronal distances $>3R_\odot$.

In late 2009, the MESSENGER spacecraft followed a superior conjunction trajectory, just after the deep activity minimum of solar cycle 23. This alignment provided an opportunity for remote sensing of the lower corona by recording the transcoronal spacecraft transmissions. Reaching well below $2R_\odot$ in closest solar approach, the MESSENGER 2009 observations allowed sampling of coronal FR disturbances not too far from where

waves and oscillations have been studied in EUV at the coronal base [*Nakariakov and Verwichte*, 2005; *Tomczyk et al.*, 2007; *McIntosh et al.*, 2011].

Faraday rotation of a linearly polarized electromagnetic signal is the result of propagation through a magnetized plasma. Rotation of the polarization plane occurs in proportion to the integrated effects of electron concentration (number density) and magnetic field along the line of sight (LOS) from the spacecraft to the terrestrial receiver. The rotation is given as a change in polarization position angle $\Delta\chi$ related to radio signal wavelength λ by $\Delta\chi = \lambda^2 RM$ where the rotation measure (RM) is

$$RM = \frac{e^3}{8\pi^2\varepsilon_0 m_e c^3} \int_{SC}^{\oplus} n_e \overrightarrow{B} \cdot d\overrightarrow{S} \tag{1}$$

in SI units (which are used throughout), with n_e the electron concentration, $\overrightarrow{B}$ the magnetic field vector, $d\overrightarrow{S}$ the LOS path vector increment, m_e is mass of the electron, e is the elementary electric charge, ε_0 is the vacuum permittivity, and c is the speed of light.

Here we clarify that we are using the convention that a positive LOS-aligned magnetic field component is directed toward the terrestrial observer and would produce a positive FR corresponding to the polarization position angle rotating counterclockwise as viewed on Earth in accordance with the right-hand rule. There is potential confusion in defining polarity of the LOS-aligned magnetic fields since in solar physics it is customary to denote a magnetic field line outwardly directed from the solar surface as being positive. An outwardly directed solar magnetic field may produce both positive and negative components on the LOS, depending on the orientation of the field relative to the LOS. Our definition for a positive $\overrightarrow{B}$ component on the LOS follows the convention of pulsar radio astronomers, in which a positive magnetic field vector points toward the observer and produces a positive rotation measure [*Hamaker and Bregman*, 1996]. It must be noted that this is opposite to official Institute of Electrical and Electronics Engineers and International Astronomical Union conventions, for which a positive field points away from the observer [*Institute of Electrical and Electronics Engineers*, 1969].

The Faraday rotation (FR) is thus the integrated result of changing magnetic fields and electron densities throughout the plasma along the full LOS from spacecraft to the Earth ($\oplus$). Since the baseline solar magnetic fields and electron densities are expected to roughly follow power laws on heliocentric distance, the FR effects in the quiescent Sun are generally dominated in the region where the LOS passes closest to the solar surface. Changes in both electron density and magnetic field contribute to the observed polarization position angle rotation, so the FR technique taken independently cannot differentiate magnetic field contributions from those of the electron concentration. Nevertheless, FR techniques can be compared with models and thus provide a valuable insight into the dynamics of coronal plasma. Techniques being developed for determination of electron number density and its fluctuations [*Jensen et al.*, 2016; *Mancuso and Garzelli*, 2013; *Kooi*, 2016] will complement FR studies and allow better constraints on the inferred B measurements.

The extensive data sets from the HELIOS 1 (1974-84) and HELIOS 2 (1976–1980) spacecraft were used to study coronal FR, the first set for large-scale coronal magnetic field structure [*Pätzold et al.*, 1987] and both sets for detailed analysis of FR fluctuations (FRFs) in transcoronal radio sounding experiments [*Efimov et al.*,1993; *Chashei et al.*, 2000; *Bird*, 2007]. *Chashei et al.* [1999] and *Efimov et al.* [2000] described intermittent segments of quasi-harmonic FRF along with power spectral wave-scale organization generally consistent with the energy cascade concept. One particularly interesting feature was the presence of 5 min wave-like oscillations in FR that appeared in up to 25% of the recordings obtained at heliocentric solar offsets above $3R_\odot$. Low-frequency FR fluctuations with time scales up to hours are believed to represent Alfvén waves [*Hollweg et al.*, 1982] and have been implicated in the overall process of energy transport required for heating and acceleration of the solar wind [*Chashei*, 1989; *Hollweg et al.*, 2010]. Recent reviews by *Efimov et al.* [2015a, 2015b] illustrate a broad range of FRF frequencies, from milliHertz (mHz) scales extending into the sub-mHz range.

A lower limit on solar offset for FR observations is set by the level of solar sidelobe noise at the receiving antenna as well as the transmitting frequency. The FR from HELIOS radio transmissions at 2.3 GHz could be resolved generally to about $3\ R_\odot$, and at best down to $R_\odot$. Since FR is proportional to the inverse square of signal frequency, modern high-frequency spacecraft radio systems operating at 8 GHz (X band) with high-gain antennas are potentially able to penetrate deeper into the corona before the signal is lost or the rate of rotation becomes unresolvable.
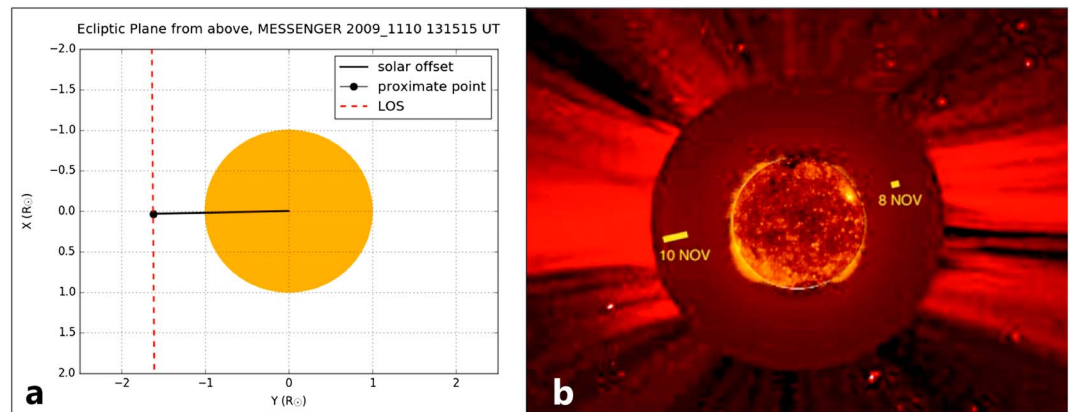
Figure 1. Geometry of the MESSENGER observations. (a) View of the ecliptic *X-Y* plane from above, illustrating a LOS together with its proximate point and the heliocentric distance to that point (solar offset). Here the solar offset is 1.65 $R_\odot$. (b) The progression in location of the proximate points is superimposed on a LASCO C2 image of the corona from 10 November 2009. The image is oriented with solar north directly upwards. A SOHO EIT 304 Å image of the Sun for the same date is placed over the location of the solar disk. The edge of the coronagraph occluding disk marks 2 $R_\odot$ (The images were obtained from the SOHO public archive, http://sohowww.nascom.nasa.gov).

Jensen et al. [2013a, 2013b] reported the FR results for MESSENGER spacecraft transmissions during the superior conjunction of November 2009. The 8.4 GHz MESSENGER radio permitted FR study deep into the corona, to about $1.6R_\odot$ (Figure 1a). They documented the broad, sloping curve of FR expected for the declining plasma density and mean magnetic field strengths with increasing solar offset. Also, evidence for 0.6 mHz waves was presented. In this report we present a further analysis of the data from 10 November 2009, covering heliocentric distances 1.6–1.9 $R_\odot$. Our data give information on the near-equatorial corona at close offset during relative solar quiescence. Techniques were developed for the reanalysis-improved resolution and permitted detailed investigation of FR fluctuations in the millihertz regime.

2. Observations and Data Processing

2.1. MESSENGER Spacecraft Observations

Observations were conducted on 8 and 10 November 2009. The Sun was still in a fairly quiescent state after the end of cycle 23, which had exhibited the longest solar minimum in a century. This state of generally low solar activity was confirmed by examining SOHO extreme ultraviolet imaging telescope (EIT) images in 304 Å, 171 Å, and 195 Å. The streamer belt pattern expected for solar quiescence was confirmed on Large Angle and Spectrometric Coronagraph (LASCO) C2 white-light coronagraphs, and the data for 10 November used in this study were found to map inside the margin of the LASCO C2 occluding disk, beneath a streamer region (Figure 1b).

At that time the MESSENGER spacecraft was on a Mercury flyby trajectory, with the path approaching the western limb of the Sun for the 8 November observations and receding from the eastern limb (solar conjunction egress) during the 10 November observations. Using position vectors for Earth, Sun, and MESSENGER obtained from the Jet Propulsion Laboratory Horizons ephemerides, the line-of-sight (LOS) path was specified for each second in heliocentric ecliptic coordinates. Heliocentric distances to the LOS point of closest approach (hereafter, proximate point) ranged 1.49–1.04 $R_\odot$ for ingress observations and 1.63–1.89 $R_\odot$ for egress. Due to signal loss at progressively deeper levels of the corona during ingress, the useful FR data were limited to 1200 s segment from solar offset 1.51 $R_\odot$ during ingress on 8 November, insufficient to include in the present work. The egress data could be processed as a nearly continuous FR record over 14,400 s and constituted the data presented here. Heliolatitude for the LOS proximate point in ecliptic coordinates was about −6°. In heliographic coordinates, the solar latitudes for the proximate point ranged −6° to −7° during egress.

The MESSENGER spacecraft was built with a high-gain antenna system transmitting at 8.4 GHz in right circular polarization (RCP) [*Srinivasan et al.*, 2007]. Pure circular polarization corresponds to an axial ratio of unity for the orthogonal linear electric vectors, meaning no intrinsic linear polarization and therefore no

capability to detect FR. However, the MESSENGER transmitter system exhibited a small departure from this ideal state at the nominal operating frequency [*Stilwell et al.*, 2003] corresponding to linear polarization of about 11%, or sometimes more depending on propagation effects. This value is comparable to percentage linear polarization established for extragalactic sources used in prior FR studies [e.g., *Ingleby et al.*, 2007] and enabled us to measure FR.

All observations were obtained by using the National Radio Astronomy Observatory (NRAO) Green Bank 100 m radio telescope, which had a native dual-circular polarized feed. The two signals were down-converted to a baseband frequency and low-pass-filtered with a cutoff frequency of about 0.3 MHz. The I-Q quadrature channels for both polarizations were sampled at 5 MHz and digitally recorded with unsigned 4-bit resolution.

FR effects due to the Earth's ionosphere and magnetic field are significant in low-frequency radio polarization studies. *Oberoi and Lonsdale* [2012] reviewed RM contributions from different parts of the ionosphere and plasmasphere. We can estimate the maximum expected ionospheric FR using their estimate of $RM = -8.31$ rad m^{-2} for a zenith measurement during times of high terrestrial ionospheric electron column density. Using $FR_{max} = RM_{max} \lambda^2$ with radio wavelength of 3.5 cm, the maximum ionospheric contribution to the FR is only ~0.01 radian. Thus, the terrestrial atmospheric contributions to the observed FR was expected to be small.

2.2. Data Processing

RCP and LCP signals were reconstituted from the complex number sequences in the science data files. The data were analyzed in sequential 1 s segments. Spectral analysis of Stokes I (total intensity) was performed to identify the signal peak, then a Gaussian fit was used to estimate signal width. This center frequency and Gaussian fit were used to obtain the power products RR*, LL*, and RL* (R = RCP, L = LCP; the asterisk denotes complex conjugate) and thereby calculate the remaining Stokes parameters Q, U, and V. Stokes Q and U were used to obtain the polarization position angle χ each second as

$$\chi = 0.5 \arctan \frac{U}{Q} \qquad (2)$$

The mean Stokes V, circular polarization, expressed as a fraction of total power (Stokes I) was 0.95. Mean fractional LCP power was 2.6%, adequate to obtain position angles of polarization. Depending on depth into the corona, the RL* cross spectrum, used to obtain Stokes Q and U, had a signal-to-noise ratio ranging 5–20.

A computational unwrap method was used to remove the $\pm n\pi$ uncertainty from the series of position angle results. The time series of unwrapped polarization angles constituted the uncalibrated FR curve (absolute position angle offset unknown). The parallactic angle correction was applied to the FR results.

The FR time series were subjected to spectral analysis. A power spectrum G of form $G \propto \nu^\alpha$ with frequency ν and characteristic spectral index a implies a set of waves or structures with an organized sequence of powers based on wave numbers. The power spectral index can give clues on the presence of temporal-spatial turbulence in the plasma and may indicate the development of an energy cascade that underlies wave turbulence models of coronal heating. FRF spectra from the HELIOS missions have shown power spectra over the ~1–10 mHz range with a about −1.6 at 6 $R_\odot$ with spectral steepening to −2.4 at 2 $R_\odot$ [*Efimov et al.*, 2015a, 2015b]. We therefore sought to confirm the presence of a power spectrum in the millihertz frequency range and obtain the spectral indices below solar offset 2 $R_\odot$.

Spectral analysis was also used to search for quasiperiodic fluctuations appearing as peaks superimposed upon the general power spectrum. Waves of period ~5 min (3–3.5 mHz) were of particular interest due to prior descriptions of this periodicity in both EUV studies at the coronal base and transition regions [e.g., *Tomczyk et al.*, 2007; *McIntosh et al.*, 2011], and in coronal FR studies beyond $3R_\odot$ [*Chashei et al.*, 1999; *Efimov et al.*, 2000].

Study of FR fluctuations in the millihertz range was facilitated by removal of the general slow trend (see section 3.1). For slow-trend removal we applied a fourth-order Butterworth high-pass filter with cutoff frequency 0.2 mHz, suitable for our 14,400 s data segment.

Spectral processing of FR curves was accomplished by using standard Python signal-processing packages. The mean noise floor, evaluated over 20–100 mHz, was extracted from the entire spectral result. A 5-point smoothing algorithm with 1:2:3:2:1 weighting was applied to the spectra. The characteristic spectral index
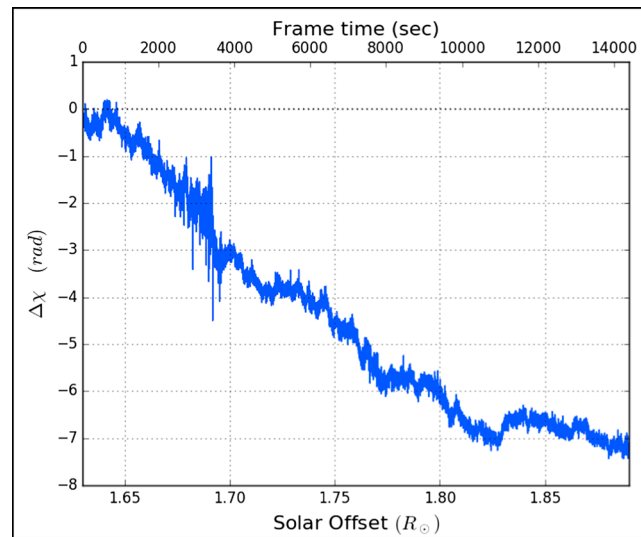
Figure 2. General trend of the Faraday rotation. The Faraday rotation over four hours of spacecraft egress from solar conjunction, starting at 13:15 UT on 10 November 2009. The phase-unwrapped polarization position angle $\Delta\chi$ decreases as egress progresses. A transient crescendo event is noted before solar offset 1.7 $R_\odot$.

α was obtained from the linear regression of log-log power versus frequency. The frequency range for determination of the power law index was adjusted as the data were assessed; details are given with rationale in the pertinent sections of the results.

To determine statistical significance of peaks in the power spectra, reference levels of variability were needed. The variability in power spectral points was quantified as the difference of power logs, $\Delta G \equiv \log G(v) - \log G_{\text{index}}(v)$, where $G(v)$ is the power spectral density (PSD) at frequency v and $G_{\text{index}}(v)$ is the idealized PSD obtained from the spectral index for that frequency. We created a randomized wave system simulation to address this matter (section 3.2).

3. Faraday Rotation Results

3.1. Faraday Rotation (FR) General Trend and Fluctuations

The overall pattern of FR over 4 h during egress, starting at 13:15 UT on 10 November 2009, is shown in Figure 2. Starting with initial polarization position angle arbitrarily set to zero, the unwrapped position angle curve broadly decreases by about 7.4 rad with a curved downtrend that shows superimposed oscillations and fluctuations. This far exceeds the expected maximal ionospheric contribution to the observed FR. A transient crescendo event that appears in the first quarter of the time series will be addressed in section 3.3.

Generally, we expect the slow downward trend in FR with increasing solar offset to be based on the LOS moving through an asymmetric large-scale magnetic field structure with declining electron concentrations. However, for our observations, which involve a dominance of high-power, low-frequency waves, a portion of the baseline offset and slow trend evolution might be due to randomized wave behavior (see section 3.2).

The change in polarization position angle shown in Figure 2 may be interpreted as at least 7.4 rad of FR produced in the LOS with proximate point at 1.63 $R_\odot$. This corresponds to RM = 6000 rad m^{-2} or greater, which dwarfs any possible contribution from the ionosphere. Of note, our large RM value is considerable greater than the 3500 rad m^{-2} maximal predicted value obtained in the empirical formula provided by *Spangler and Whiting* [2009]. Their maximal value is obtained based on radial magnetic fields with polarity reversal region (referred to as a sector boundary or neutral line) near the proximal point [see also *Ingelby et al.*, 2007; *Kooi et al.*, 2014]. The opposite condition, in which there is no fairly nearby polarity reversal in an otherwise radial field, would result in minimal net FR due to cancelation of mirror image rotation contributions along the LOS with respect to the proximate point. We reviewed the Coordinated Community Modeling Center (CCMC) Magnetohydrodynamic Algorithm on a Sphere (MAS) polytropic model (http://ccmc.gsfc.nasa.gov/models) generated for 10 November 2009 to locate the angular position of the magnetic neutral line at approximately 30° relative to the line from heliocenter out to the LOS proximate point. Most likely, our results point to asymmetric, nonradial magnetic fields, and deviation from simple radial power law relationships for magnetic field strength at this coronal level. To follow up on these impressions, we plan to scrutinize magnetic field strength and electron concentrations along the LOS paths using 3-D MHD models for comparison with the observations [e.g., *LeChat et al.*, 2014].

As seen in Figure 2, irregular fluctuations, with various time scales, are found superimposed on the general FR slow trend. Analysis of these fluctuations provides a basis for understanding the purported Alfvén waves believed to play a key role in coronal magnetic energy transport. FR fluctuations are studied by first isolating
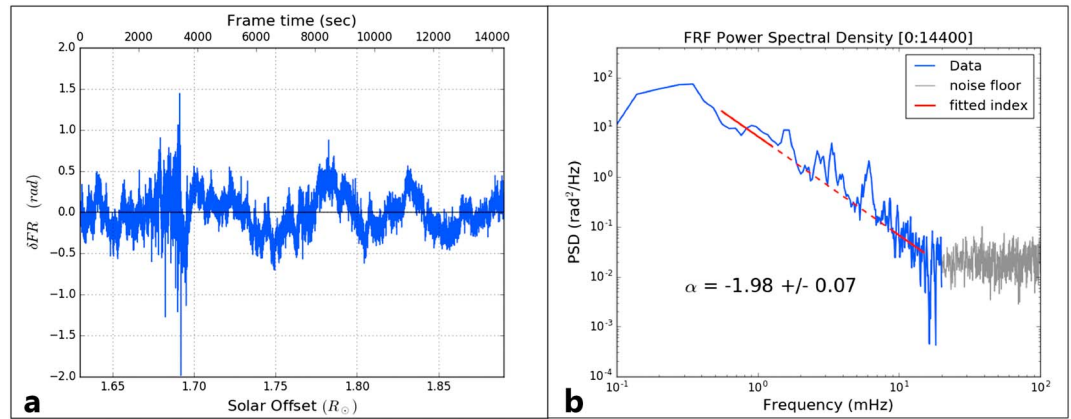
Figure 3. FR fluctuations from observations of MESSENGER radio signals, 10 November 2009. (a) The FR fluctuation time series, obtained by high-pass filtering with a frequency cutoff of 0.2 mHz. Fluctuations are seen across the record, with a transient crescendo event noted in the first quarter of the time series. (b) Power spectral density (PSD) analysis of the FR fluctuations (blue), after subtraction of the mean from the flat spectral floor (gray). The power law index line was fitted over 0.5–1.3 mHz and 9–15 mHz bands (thick red lines) to avoid influence of the apparent spectral enhancements in the central millihertz range (dashed red line). Possible spectral peaks noted around 1.5, 3.5, and 6 mHz were subjected to further study to assess statistical significance.

the variations from the underlying baseline trend [*Song and Russell*, 1999]. We remove the baseline trend (hereafter, detrend) to isolate the frequency domain of interest for the particular question. Here we are interested to learn about FRF initially in the range 0.5–20 mHz.

The common methods for time series detrending are subtraction of a second- or third-order polynomial fit across the given analysis frame, and high-pass filtering (HPF). We studied both methods and found that each had drawbacks: the HPF resulted in phase shifts and temporal distortion of the time series, while preserving the desired frequency range and avoiding spurious presentation of frequencies below the cutoff. Polynomial detrending preserved the time relationship of peaks in the time series (no phase shifts) but had variable and somewhat unpredictable effects on the power spectrum. We had a particular interest in the power spectrum, and therefore ultimately chose to remove the low-frequency trend using HPF to achieve a well-characterized spectral response. The phase shifts from filtering do not degrade the power spectral analysis.

The FR fluctuation time series was obtained by high-pass filtering with a frequency cutoff of 0.2 mHz. Fluctuations are seen across the record, with a transient crescendo event noted in the first quarter of the time series (Figure 3a). The FR fluctuation time series individual elements may be denoted δFR, and the mean square across the time series as $\langle\delta\text{FR}^2\rangle$ where the angle brackets denote an average. The square root of this value is the root-mean-square (RMS). For the data in Figure 3a, the FRF RMS is 0.23 rad. Converted to the HELIOS 2.3 GHz carrier signal, the equivalent RMS is 3.0 rad rotation, which matches fairly well the expected value for a low-latitude streamer region in the HELIOS results (see Figure 3 in *Hollweg et al.* [2010]). The FRF RMS estimate will be useful in calculating Alfvén wave energy flux density for the model developed in section 4.

The observed FR fluctuations are not attributed significantly to ionospheric variations. About 90% of the Earth's atmospheric FR occurs in the ionosphere. Various ionospheric disturbances on time scales of minutes to hours may have associated RM of on the order of 0.1 rad m^{-2}, while day-to-day variability may reach 0.3 rad m^{-2} [*Oberoi and Lonsdale*, 2012]. Sporadic storm-enhanced densities (SEDs) may boost electron concentrations greatly in the upper ionosphere and above, with resulting RM up to 6 rad m^{-2} over a timescale of minutes to hours. Even in the case of an extreme SED event, the expected variation of FR for our X-band data is ~0.01 rad, or about 4% of the observed large-wave amplitudes.

The PSD plot for the FRF is given in Figure 3b. A power law relation appears over frequency range approximately 0.3–20 mHz, and a flat spectral floor is noted above 20 mHz. The RMS power of this spectral floor over 20–100 mHz was subtracted from the spectrum before calculating the power law spectral index. The spectral flattening below 0.3 mHz is expected from the filtering with cutoff frequency 0.2 mHz. Due to these upper and lower frequency bounds on the power law region, as well as the localized enhancements of spectral
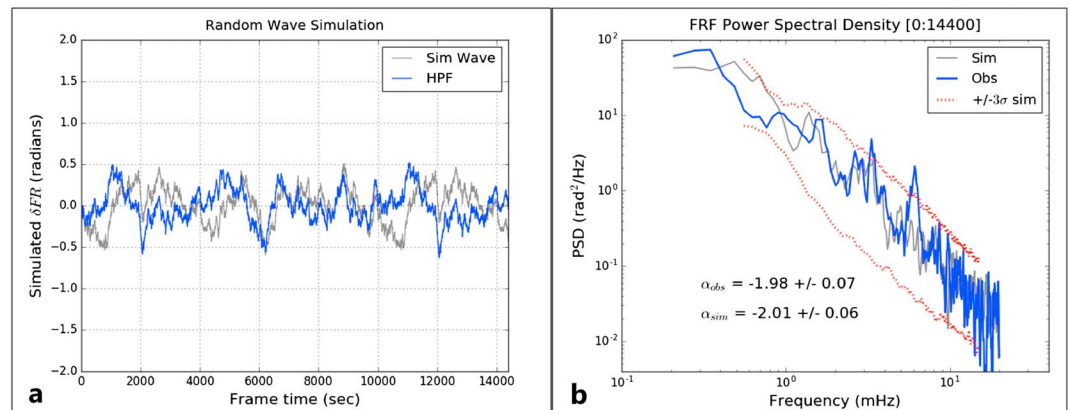
Figure 4. Simulated system of randomized oscillators and the MESSENGER FRF. (a) The simulation time series of random fluctuations (in gray) has been processed by high-pass filtering, with the resulting waveform in blue. Filtering produces frequency-dependent phase shifts. (b) The power spectrum of the MESSENGER observations (blue) are coplotted with a sample simulation spectrum (gray). The upper and lower three standard deviation limits determined by 300 simulation trials are shown (dotted line). The MESSENGER data show spectral enhancement at 3.3 and 6.1 mHz, with <1% probability of random chance occurrence.

power around 1.5, 3.5, and 6 mHz, we elected to determine the power law spectral index as follows. For the lower end of the power law fit, the 0.5–1.3 mHz range was used, and at the upper end, the 9–15 mHz range. The spectral index was calculated by linear regression on the double log plot, using only the upper and lower regions above for the fitting. The spectral index, with standard error, was found to be -1.98 ± 0.07.

Statistical evaluation of the spectral peaks at ~1.5, 3.5, and 6 mHz required study of random fluctuations in the power spectrum and the potential computational artifacts of detrending the time series data. These issues are addressed in the next section.

3.2. Monte Carlo Simulations

Simulated time series of random fluctuations based on a v^{-2} power spectrum (spectral index $\alpha = -2$) were generated to study the power variations expected on a random statistical basis. The main purpose was to determine the threshold for which a given peak in the observed MESSENGER FR spectrum had no more than a 1% chance of being due to random chance in the time series of fluctuations. Also, the simulations were used to address the expected outcomes from processing of shorter data segments, e.g., 3600 s. These shorter analysis segments were of interest to examine temporal changes in spectral index and FRF RMS values across the full data record.

A system of 1000 oscillators was generated computationally, with frequencies distributed evenly over 0.2–100 mHz. The oscillators were initially scaled to v^{-1} amplitude, then randomized in phase and subjected to an additional randomized amplitude scaling factor [*Timmer and Köenig*, 1995]. Oscillator outputs were then summed to produce simulated time series of length 14400 s. This time series was processed with the same high-pass filtering parameters as used with the MESSENGER data. A histogram of the resulting simulation fluctuations showed reasonably Gaussian distribution of fluctuations. The final amplitude scaling was applied to force the simulation RMS amplitude to 0.23, matching the FRF RMS of the observational data. A set of three hundred such simulated time series was analyzed to obtain the summary statistics for power law spectral index and ΔG for each frequency bin. The ΔG statistics were used to quantify the intrinsic variability exhibited in the power spectrum of the randomized oscillator system.

We found that a sum of randomized waves with power scaled as v^{-2} can occasionally produce a baseline offset that persists for some time. Therefore, in time-limited analysis frames, a given observed baseline offset may include both the intrinsic physical offset and that introduced via randomized low-frequency oscillatory components. For our observations, random behavior in the high-power, low-frequency waves could account for a portion of the baseline offset and slow trend evolution. This effect is attenuated by high-pass filtering, which was used for study of the FR fluctuations.

A sample 14,400 s simulation is shown as the gray curve in Figure 4a. The phase-shifting effects of high-pass filtering (blue curve) are apparent in the lower frequencies.
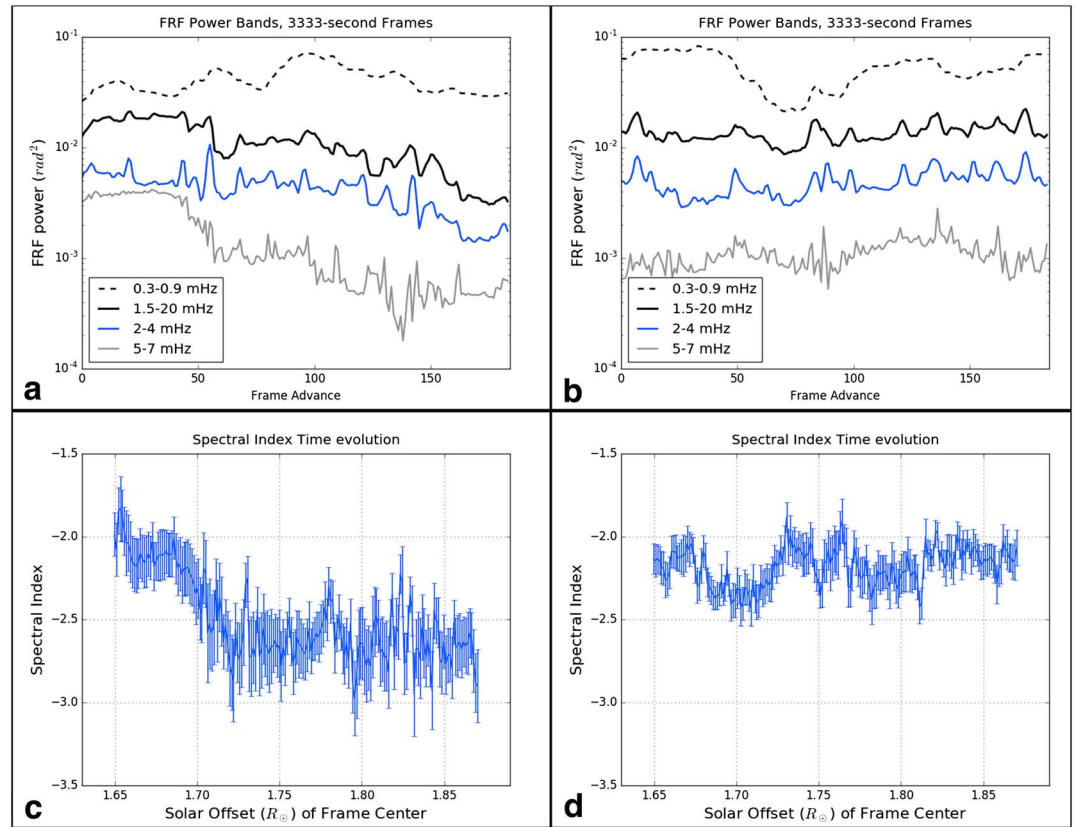
Figure 5. Sliding Frame analysis. (a) Power band analysis for the observations, using sequential, overlapping analysis frames of length 3333 **s**. Each frame advance positioned the start of next analysis frame 60 **s** after the previous frame start. FRF power in bands 0.3–0.9, 1.5–20, 2–4, and 5–7 mHz are shown. The 1.5–20 mHz band power decreased with increasing solar offset. The 5–7 mHz band shows greatly increased power in the first quarter of the record. The 0.3–0.9 mHz band shows wide variability and lack of an overall downtrend with increasing solar offset. (b) The power band analysis for a simulation time series. No overall downtrends noted. (c) Power law spectral index time evolution for the observations. A clear shift downward below index −2.5 occurs between the first quarter of the record and the remainder of the data segment. (d) Spectral index time evolution for the simulation. The spectral index is largely confined between −2.0 and −2.5.

The power spectrum for the sample FRF simulation is shown in gray in Figure 4b, with 3 sigma limits based on 300 trials. The spectrum from our observations is coplotted in blue. Comparing the observational results to those from the simulation, we found no significant difference in spectral indices, -1.98 ± 0.07 for the observations versus -2.04 ± 0.14 for the set of 300 simulation trials. The spectral peaks at 3.3 mHz and at 6.1 mHz in the observations are considered statistically significant, below 1% chance of random occurrence.

Interpretation of the 14,400 s spectrum is complicated by the consolidation of varying physical conditions over 4 h, and over 200,000 km (0.29 $R_\odot$) change in closest solar approach, into a single composite spectrum. A crescendo FRF transient is observed in the first quarter of the record, while the remainder of the time series suggests more stationary processes. The finding of peaks at 3.3 and 6.1 mHz raised the possibility of quasiperiodic components (nearly monochromatic transient wave trains) in the record, motivating a closer search through the time series. Changes in spectral structure were therefore investigated by interval analysis to explore radial dependencies and to search for more homogenous snapshots of coronal activity.

3.3. Interval Analysis and Radial Dependencies of Faraday Rotation Fluctuations

A sliding window algorithm was applied to the observed FRF time series as well as the simulated time series. We decided on a frame length of 3333 mHz to allow capture of oscillations down to 0.3 mHz. The analysis proceeded as a succession of advancing, overlapping windows, with each successive window advancing 60 **s** over the last. For the observations, frame advance corresponds to increasing solar offset. In each frame, spectral index and FRF power for three different frequency bands were determined and plotted as functions of

frame advance (Figure 5). FRF power within each frequency range v_1 to v_2 was obtained from the power spectral density $G(v)$ by integrating over the specific frequency band

$$P_{\mathrm{FRF}} = \sum_{v_1}^{v_2} G(v)\Delta v \qquad (3)$$

We studied the time evolution of power for various frequency bands and found that for these observations, the band below 1 mHz had different behavior than the bands greater than 1 mHz (Figure 5a). No specific trend was found in the simulation sliding frame analysis (Figure 5b). In both Figures 5a and 5b, the 0.3–0.9 mHz power band shows wide variations but no definite upward or downward trend during increasing solar offset. In contrast, the 1.5–20 mHz band for observations did show a downward trend with increasing frame advance, but the simulation did not. When the power law spectral index was determined over range of 0.3–20 mHz, the values fluctuated wildly due to the large swings in <1 mHz power, but when the spectral index was determined in the 1.5–20 mHz range (Figures 5c and 5d), the trends were more stable. We concluded that the 1.5–20 mHz frequency band can be conveniently treated as a unit for purposes of spectral index determination and tracking organized spectral power. Accordingly, we re-assigned the bins for fitting the spectral index to 1.5–3.0 mHz for the low end and 10–20 mHz at the high end and used these for the remainder of the analysis. The intermediate (>3, <10) mHz range was left out of the spectral index fitting to avoid distortion from the spectral peaks described in section 3.2.

Three main points emerge from the sliding frame analysis. First, the sub-mHz power fluctuations dominate the overall power and do not seem to mirror the decline in power over advancing frames (that is, over increasing radial offset) that is seen with the 1.5–20 mHz power band. The large sub-mHz fluctuations in this data segment may represent a different underlying physical process. Further data will need to be evaluated to follow-up on this finding. Second, in 1.5–20 mHz band there is a general downward trend of fluctuation RMS with increasing solar offset, with an occasional overlay burst of power. The third point is that the first quarter of the record shows a different spectral index than the rest of the record and should be studied as a separate data unit (Figure 5c). Reinforcing this point is the finding that power in the 5-7 mHz range was preferentially boosted in the first quarter of the record (Figure 5a, in gray) compared to the 1.5–20 mHz band.

A high-detail view of the first-quarter FRF segment is shown in Figure 6a. Quasiperiodic oscillations with a period on the order of 200 s are noted. The FRF amplitudes increase near the end of the frame. The associated power spectrum is shown in Figure 6b, with ± 3 standard deviation limits obtained from 300 wave simulation trials processed identically. Spectral peaks at 3.3 mHz and 6.1 mHz surpass the threshold for significance at the 1% level. Compared to the FRF in the remaining three quarters of the time series, the spectral index is relatively flattened to -1.79 ± 0.17. As seen in Figure 5c, the spectral index then becomes ~ -2.2 reflecting the sliding analysis frames containing portions of both transient and nontransient data. After frame advance 50, the spectral index remains largely below -2.5, no longer influenced by the first-quarter transient event.

The time series and power spectra for the remaining three quarters of the FRF record are given in Figures 6c and 6d. The three spectra were similar and generally confined within the 3 standard deviation envelope. The mean spectral index was -2.64 ± 0.12. There were no peaks in the 1–10 mHz range surpassing the 1% thresholds for statistical significance, although borderline peaks just above 10 mHz were noted.

4. Discussion

4.1. Faraday Rotation Fluctuations (FRFs)

The MESSENGER 2009 radio data provided high-resolution Faraday rotation results for solar offset range 1.63–1.89 $R_\odot$ near solar minimum. We found overall concordance with previous coronal sounding FR studies that had been conducted with longer radio wavelengths, greater solar offsets, and different recording equipment. Initial comparisons are now presented.

The FRF power spectrum (Figures 3 and 6) showed a power law form similar to that found in the HELIOS studies [*Efimov et al.*, 2015b; *Bird*, 2007; *Efimov et al.*, 2000]. We found it useful to separate the data analysis frame with the transient event from those showing only the general background fluctuation spectrum. For the latter, a mean spectral index of -2.64 ± 0.12 characterized the power in frequency band 1.5–20 mHz. *Efimov et al.* [2015a] reported an FRF spectral index (here presented as a negative value) of -2.4 ± 0.2 at 2 $R_\odot$ and a trend of decreasing magnitude with increasing distance. Our determination of $\alpha = -2.64$ seems a
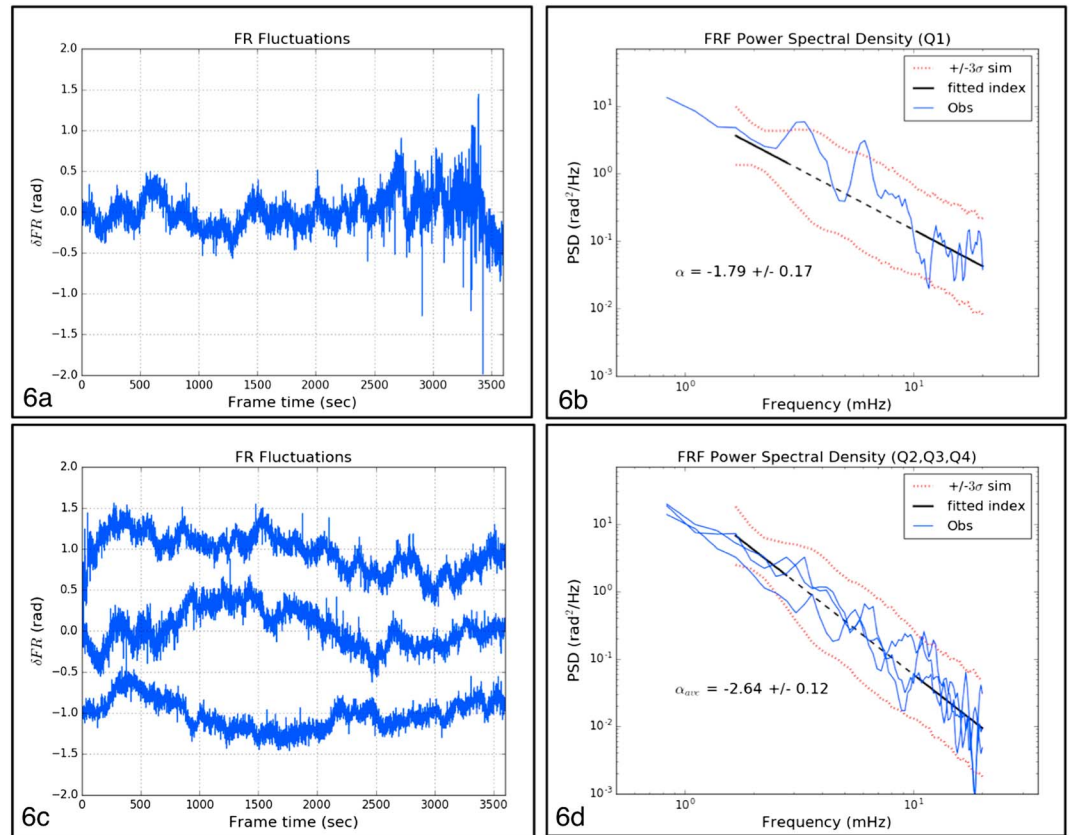
Figure 6. FR fluctuation analysis in 3600 s frames. (a) FRF time series of the first quarter (Q1), showing the transient crescendo event. Fluctuations with periods on the order of 200 s are seen, and increased amplitudes in the second half of the analysis frame. (b) Spectral analysis of FRF Q1 shows spectral enhancement at 3.3 mHz and 6.1 mHz, significant beyond 3 standard deviations (dotted lines). The spectral index is flattened to −1.79. (c) FRF time series for the three remaining 3600 s segments (Q2, Q3, and Q4) in the observations. For clarity, Q2 (top curve) is plotted with offset +1 rad, and Q4 (bottom curve) is plotted with offset −1 rad. (d) Power spectra for Q2, Q3, and Q4. The average spectral index is steepened to −2.64 ± 0.12. The spectra are generally confined within the error limits (dotted lines) although borderline peaks can be seen just above 10 mHz.

credible extension of their spectral index curve to solar offset ~1.6–1.9 $R_\odot$. We note that this spectral index value is close to the theoretical spectral index −8/3 which results from LOS integration of a Kolmogorov-like 3-D local turbulence spectrum [*Chashei et al.*, 2000]. Overall, we found that the background power spectrum over ~1–20 mHz was consistent with a system of randomized magnetic waves and suitably scaled for a turbulent process; we will proceed with the hypothesis that the FRFs are due to wave-like fluctuations.

Behavior of the background magnetic wave spectrum is further illustrated in the radial dependency of FRF RMS amplitude (Figure 7). A sliding window analysis of frame length 200 **s** was applied sequentially through the data, providing essentially a running average of FRF RMS. We see that the FRF RMS values increase by a factor of ~2 during the crescendo transient in the first part of the record. Lesser transient surges are seen thereafter. The apparent FRF RMS baseline trends downward gradually with increasing solar offset. Interestingly, when the radial behavior of total electron content (TEC, or column density) is overplotted (Figure 7, dashed line), the "floor" of background fluctuations tracks the TEC trend line fairly well. Here we computed the electron concentration using the radio data of *Mercier and Chambe* [2015]. Fitting their data for the equatorial Sun over 2008–2010, we obtain

$$n_e(r) = 1.11 \times 10^{14} r^{-6.83} \tag{4}$$

where r is the heliocentric distance in solar radii and the electron number density is in m^{-3}; their data extend only to ~1.5 $R_\odot$, but we will use equation (4) to extrapolate the electron concentration to
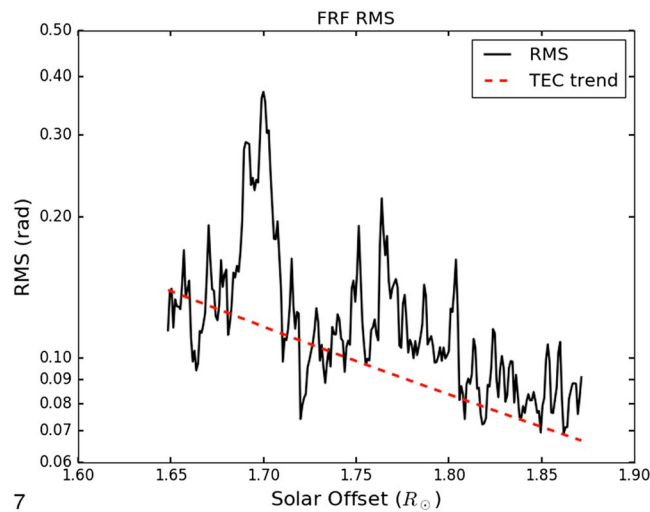
Figure 7. Radial dependency of FRF RMS. FRF RMS values are shown in consecutive 200 s frames. The FR fluctuations diminish in amplitude with increasing solar offset. The floor of RMS values roughly parallels the slope of the estimated total electron content (TEC, dashed line), while the surges also diminish but not in parallel to the TEC curve.

modestly greater distances. This formula gives a lower estimate at the proximate point than the standard Allen-Baumbach formula for the quiescent solar corona [*Allen*, 1947; see also *Bird and Edenhofer*, 1990], possibly due to the observations being taken just after the unusually deep solar minimum of solar cycle 23. It was felt that electron concentration data specific to our observation time frame would be more appropriate than use of a general parameter formula.

The TEC was then obtained computationally by integrating segments along the LOS out to 3 $R_\odot$ to either side of the proximate point, capturing most of the electron density. A uniform pattern of magnetic fluctuations should result in FRF that scale down with increasing solar offset due to decreasing electron concentration; see equation (8) below. Our finding that the FRF RMS and the TEC follow similar trends supports the concept of broadly distributed randomized magnetic waves in this region of the corona.

Our work demonstrates low-frequency FR fluctuations in the lower corona but does not prove the existence of propagating waves since we had only single-station observations. FR studies using two-station temporal cross correlations did show evidence for wave propagation [*Bird*, 2007; *Efimov et al.*, 2015b; *Jensen and Rusell*, 2009]. Below the Alfvén critical point, where the Alfvén speed exceeds the solar wind speed, the two-station data indicated propagation sometimes toward but mostly away from the Sun. Bidirectional wave transmission is important in MHD wave energy dissipation.

The present study supports the concept of a field of randomized fluctuations on the background magnetic field. When we ran the simulated oscillator system, a number of features of such a field were reproduced. *Hollweg et al.* [1982] found that FR fluctuations were due mostly to variations in magnetic field strength rather than density changes, suggesting that the fluctuations were due largely to Alfvén waves. Other studies [*Andreev et al.*, 1997; *Efimov et al.*, 2015a; *Bird*, 2007] also support the interpretation of FRF as coronal Alfvén waves. The role these waves may play in solar wind acceleration is still being evaluated by the solar physics community [see *Roberts*, 2010]. *Mancuso and Spangler* [2000] consider the possibility of relatively static coronal structures moving through the LOS to explain very low-frequency FR perturbations. We suggest the possibility that while a spectrum of randomized waves may permeate the coronal magnetic fields in the 1–20 mHz range, the high-power lowest-frequency FR components may have a different physical basis, e.g., random shifting of the photospheric footprints that could reconfigure the overall field structure, at least in the lower corona. These questions can be explored by studying combined data sets that cover a wider range of solar offsets, solar latitudes, and phases in the solar cycle.

The transient event seen in the first part of the data contained narrow-band spectral enhancement with peaks at 3.3 and 6.1 mHz (Figures 6a and 6b). The 3.3 mHz peak corresponds to intermittent quasi-harmonic oscillations of ~5 min period reported by *Efimov et al.* [2000] and *Chashei et al.* [1999] for FRF observations beyond 3 $R_\odot$. The finding of augmented power at ~6 mHz is interesting because it might indicate MHD wave harmonics. *Mathioudakis et al.* [2013] point out that the energy of Alfvén waves propagating in a turbulent medium can be transferred to other wave modes (i.e., magnetosonic) and may appear as a first harmonic peak in the power spectrum [see also *Jensen*, 2007]. Harmonic power spectral features are found in the earlier studies of HELIOS, e.g., 6–7 mHz enhancement [*Efimov et al.*, 2000, Figure 3] and 12–15 mHz [e.g., *Bird*, 2007, Figure 12; *Efimov et al.*, 2000, Figure 1]. The FR imprint of millihertz wave-like activity in the lower corona is unequivocal, but further study is required to clarify FRF physical significance and relation to solar wind acceleration mechanisms.

Jensen et al. [2013b] reported spectral enhancement at 0.625 mHz and possible enhancements at 1.68 and 4.49 mHz for the same MESSENGER 10 November 2009 data we analyzed here using different methods. As discussed in section 3.1, spectral results are highly sensitive to the specific detrending and filtering methods used. While we confirm visually in Figure 3a large-amplitude waves with periods around 2000 **s** (0.5 mHz), using the present methods no significant power excess in the 0.4–0.6 mHz range was found in the power spectrum (Figure 4b); the low-frequency waves are already dominant as a consequence of the power law spectral organization. We found a nonstatistically significant spectral enhancement at ~1.5 mHz, corresponding to the peak described by *Jensen et al.* [2013b], but no features to corroborate the 4.49 mHz finding. Our analysis was carried out with higher temporal resolution than that of the earlier work, and when confined to the interval near the transient event, demonstrated more clearly spectral enhancements in the 3–6 mHz range (Figure 6b). *Jensen et al.* [2013b] removed the low-frequency trend using a time series smoothing algorithm [*Sakurai and Spangler*, 1994], which accomplished high-pass filtering but with uncertain spectral properties. We applied Butterworth high-pass filters with known spectral characteristics and are confident that the methods can be reliably extended to further studies of coronal FR.

4.2. Wave Energetics

FRF RMS values can be used to obtain a rough estimate of magnetic wave energy flux, under the assumption that the FRF are due solely to fluctuations of the magnetic field crossing the LOS [*Hollweg et al.*, 1982]. We further assume that the fluctuations are caused by Alfvén waves propagating outward along radially directed magnetic field lines in the high-frequency (WKB) limit. In this idealized case of radial symmetry, the background magnetic field contributions along the LOS cancel out across the proximate point, but the transverse Alfvén waves propagating radially may contribute magnetic components along the LOS without cancelation. These randomized waves are expected to be uncorrelated and therefore may be summed along a given LOS as a random walk. Only waves having nonzero LOS-alignment add to the observed FR. These randomized waves are expected to be uncorrelated and therefore may be summed along a given LOS as a random walk. Finally, we assume that most FRFs originate near the proximate point where the plasma density is greatest. Since only the LOS-aligned magnetic fluctuations contribute to the observe FRF, it is likely that only a fraction of the total wave power is being captured in the radio observations.

We denote the Alfvén wave magnetic perturbation as δB, and the energy flux density (Poynting flux) as

$$F_{wave} = \frac{1}{\mu_0} \delta B^2 V_A \tag{5}$$

where μ_0 is the permeability of free space and V_A is the Alfvén speed. Here δB^2 includes components both along and across the LOS. The effect of bulk plasma flow on the wave energy flux will be adressed below following equation (10).

Our first goal is to obtain an estimate of δB_{LOS} from the observed FR fluctuation

$$\delta FR = A \int LOS\, n_e \delta B_{LOS} dS \tag{6}$$

where the consolidation of constants and using signal frequency 8.4 GHz yields $A = 3.35 \times 10^{-16}$ m^2 rad T^{-1} and δB_{LOS} specifies the component of the magnetic fluctuation along the LOS, with positive being defined in the direction of the LOS increment dS toward Earth. As given, this equation assumes $\delta n_e/n_e \ll \delta B/B$.

The contribution of a single element, or "step," to the random walk summation is

$$\left\langle \delta FR_{elem}^2 \right\rangle = A^2 n_e^2 \left\langle \delta B_{elem}^2 \right\rangle L^2 \tag{7}$$

where $\left\langle \delta B_{elem}^2 \right\rangle$ is a mean-square LOS-aligned magnetic fluctuation element and L_s is the correlation length, i.e., the size of a single step. The correlation length may be approached in a number of ways. Some consider the correlation scale as roughly equal to the spacing between magnetic flux tubes [*Hollweg et al.*, 1982; *Spruit*, 1981], which can give L_s on the order of thousands of kilometers. Others [*Spangler*, 2002, *Andreev et al.*, 1997] have judged the correlation scale to be about one solar radius or more, which would give much lower estimates of δB. Here we use the interpretation given in *Hollweg et al.* [2010] equation (5a) to obtain $L_s = 5000$ km at path offset 1.63 $R_\odot$. This sets the length scale along the LOS for a single transverse Alfvén wave at the proximate point. Many such waves should be crossing the LOS at any given time, but only those fairly near the proximate point will be passing through a high enough electron concentration to affect the FR appreciably.

In the spirit of rough estimates, we take L_s, n_e, and $|\delta B_{elem}|$ to be constant along the main FR-modulating region for a given solar offset. Review of density and radial magnetic field profiles at solar offset 1.63 $R_\odot$ determined that the main contributions to the mean square FR come from ~0.4 $R_\odot$ to either side of the proximate point. We therefore take 0.8 $R_\odot$ to be the effective integration length S along the LOS. The heliocentric offset distance along this relatively short integration path varies by only ~3%. The number of elements N contributing to the random walk along the effective LOS is S/L_s. Since the random walk scales as $\sqrt{n}$, we multiply equation (7) by S/L_s to yield the expression for the summated $\langle \delta B_{elem}^2 \rangle$ that was modeled to correspond to the observed FRF RMS value:

$$\langle \delta FR_{obs}^2 \rangle = A^2 n_e^2 \langle \delta B_{elem}^2 \rangle L_s S \tag{8}$$

which is equivalent to equation (7) in *Hollweg et al.* [2010].

For a sample calculation, we take the δFR_{obs} RMS value to be 0.23 rad (from data in Figure 3a) at solar offset 1.63 $R_\odot$. The corresponding electron concentration n_e, extrapolated from *Mercier and Chambe* [2015] for the equatorial Sun over 2008–2010, was 4×10^{12} m^{-3}. The resulting RMS δB is 3.3×10^{-6} T. To obtain the energy flux density using equation (5), an estimate for the Alfvén speed

$$V_A = \frac{B}{\sqrt{\mu_0 n_e m_p}} \tag{9}$$

is necessary. Different approaches are available to estimate the local magnetic field strength B.

Pätzold et al. [1987] studied the radial dependence of B using Faraday rotation data, but their results describe the field only down to 3 $R_\odot$, too far from the Sun and too uncertain for applicability here. Similarly, *Jensen and Rusell* [2009] analyzed HELIOS FR data at offset 4 $R_\odot$, which is again too far from the Sun for our purposes. Another approach is the use of coronal 3-D models, which are produced using composite, synoptic magnetograms for a given Carrington rotation. Such models are intended for quasi-static coronal analysis, and thus pertinent for obtaining B near the proximate point. However, the coronal 3-D models typically underestimate B. *Bird and Edenhofer* [1990] reported on magnetic field strength discrepancies on the order of a magnitude. A recent report [*Jian et al.*, 2015] comparing different heliospheric models to in situ data at 1 AU indicated that scaling factors of about 5 were typically needed to bring the models in line with the direct measurements. Further studies are needed to improve the scaling and calibration of these models in the corona.

To find the approximate local magnetic field strength for our sample calculation, we used the CCMC MAS polytropic model (http://ccmc.gsfc.nasa.gov/models) for 10 November 2009, obtaining a value of 7×10^{-6} T. Applying a scaling multiplier of 5 from *Jian et al.* [2015], we obtain the estimated coronal magnetic field strength near the proximate point, 3.5×10^{-5} T. Then V_A calculates to 400 km s^{-1}, and the Alfvén wave energy flux density to 7 W m^{-2}. Note we have scaled up the flux density by a factor "2" to take into account putative Alfvénic magnetic field fluctuations that are perpendicular to the LOS. For radial magnetic field lines lying roughly in the plane of the sky, transverse waves with perturbations along the LOS (out of the plane of the sky) would contribute to the observed FRF, while those with perturbations in the plane of the sky would not. It is this latter group of waves, assumed to represent half the total, that is incorporated into the flux calculation by applying the factor of 2. If the background magnetic field lines had a substantial component along the LOS, then we would have to apply a factor greater than 2. We also note that $\delta B/B \sim 0.1$ in this analysis, which is intuitively reasonable and considered acceptable for linear perturbation models.

For comparison, the kinetic energy flux of the solar wind is

$$F_{SW} = \frac{1}{2} n_e m_p V_{SW}^3 \tag{10}$$

Using $n_e \sim 4 \times 10^{12}$ m^{-3}, and solar wind speed V_{SW} for this heliocentric offset as 50 km s^{-1} [*Imamura et al.*, 2014; *Jones and Davila*, 2009], the estimated F_{SW} in the equatorial quiescent Sun is 0.4 W m^{-2}. If we were to include this value for the solar wind flow speed in equation (5) by replacing V_A with $V_A + V_{SW}$ and also by including the convection of wave kinetic energy [e.g., *Hollweg*, 1974, equation (17)], we would obtain an increase of the wave energy flux density of about 20%. Using our simplified model it appears that low-frequency equatorial coronal Alfvén waves may convey energy at a rate above that of the local solar wind kinetic energy, although still only a fraction of that required to power full solar wind acceleration, which is at least 100 W m^{-2} when thermal and gravitational energy terms are included. However, as seen in

Figure 7, variable surges in FRF RMS may appear; a doubling of the RMS during a surge would boost the wave energy flux density by a factor of four. In addition, the results are very sensitive to changes in electron concentration and the local magnetic field strength. If L_s scales as $B^{-1/2}$ [*Spruit*, 1981], then the energy flux density modeled here scales as $B^{\frac{3}{2}} n_e^{\frac{-5}{2}}$. Even with the original modest FRF RMS of 0.23 rad, a variation in background B, scaled up by a factor of 2, and number density lowered by a factor of 2, together produce a 16-fold increase in Alfvén wave energy flux density to an energetically important ~110 W m^{-2}. Further data should be analyzed to evaluate whether our estimate of 7 W m^{-2} is truly representative.

A number of uncertainties beset the energy flux calculations, reinforcing the point raised by *Mancuso and Spangler* [1999] that the modeled wave energy is extremely dependent "on imperfectly known properties of the coronal plasma along the line of sight." Thus, progress on elaborating coronal magnetic energy transport is inherently linked to the task of constraining the coronal plasma parameters and background magnetic field intensity. This is particularly difficult in the lower equatorial corona, where complex temporally varying open and closed magnetic structures may be present. Looking forward, the 3-D synoptic coronal computational models (e.g., from CCMC) may provide the needed structural framework to create sharpened FR analyses and improved magnetic field strength and plasma density estimates. And of course everything relies on the crucial ansatz that the observed FRF are due predominantly to the magnetic fluctuations in outgoing Alfvén waves, with little contribution from plasma density fluctuations. This, at least, is consistent with earlier analyses of FRF observed using the HELIOS radio transmissions [*Hollweg et al.*, 1982].

4.3. Conclusions

In summary, we have demonstrated millihertz FR fluctuations in the lower equatorial corona near solar minimum. The fluctuations generally formed a power spectrum with a spectral index of -2.64 over frequency range of 1.5–20 mHz. Our findings are consistent with prior reports supporting the low-frequency coronal Alfvén wave interpretation. A transient crescendo event with spectral power enhancements at 3.3 and 6.1 mHz was detected. The estimated Alfvén wave energy flux density was above the local plasma bulk kinetic energy flux density but provided only a fraction of the power required to accelerate the solar wind. Even so, this fraction is quite variable and potentially escalates to energetically significant values with relatively modest changes in magnetic field strength and electron concentration. Additional FRF studies on the lower corona are desirable to further sample the range of possible wave energies and search for other transient power surge phenomena. Continued investigation is warranted to understand these FR perturbations in the broader context of coronal structure, wave transformations, and dissipation mechanisms.

References

Allen, C. W. (1947), Interpretation of electron densities from corona brightness, *Mon. Notices R. Astron. Soc.*, *107*, 426–432, doi:10.1093/mnras/107.5-6.426.

Andreev, V. E., A. I. Efimov, L. N. Samoznaev, I. V. Chashei, and M. K. Bird (1997), Characteristics of coronal Alfvén waves deduced from HELIOS Faraday rotation measurements, *Sol. Phys.*, *176*, 387–402, doi:10.1023/A:1004965310604.

Arregui, I. (2015), Wave heating of the solar atmosphere, *Phil. Trans. R. Soc. Ser. A*, *373*, doi:10.1098/rsta.2014.0261.

Bird, M. K. (2007), Coronal Faraday rotation of occulted radio signals, *Astron. Astrophys. Trans.*, *26*(6), 441–453, doi:10.1080/10556790701595236.

Bird, M. K., and P. Edenhofer (1990), Remote sensing observations of the corona, in *Physics of the Inner Heliosphere I*, edited by R. Schwenn and E. Marsch, Springer, Berlin.

Chashei, I. V. (1989), Acceleration of the solar wind by Alfvén waves, *Geomagn. Aeron.*, *29*, 718–724.

Chashei, I. V., M. K. Bird, A. I. Efimov, V. E. Andreev, and L. N. Samoznaev (1999), Five-minute magnetic field fluctuations in the solar wind acceleration region, *Sol. Phys.*, *198*, 399–413, doi:10.1023/A:1005223531849.

Chashei, I. V., A. I. Efimov, L. N. Samoznaev, M. K. Bird, and M. Patzold (2000), The spectrum of magnetic field irregularities in the solar corona and in interplanetary space, *Adv. Space Res.*, *25*(9), 1973–1978, doi:10.1016/S0273-1177(99)00614-6.

Efimov, A. I., I. V. Chashei, V. I. Shisov, and M. K. Bird (1993), Faraday-rotation fluctuations during radio occultation of the circumsolar plasma, *Astron. Lett.*, *19*(1), 57–61.

Efimov, A. I., L. N. Samoznaev, V. E. Andreev, I. V. Chashei, and M. K. Bird (2000), Quasi-harmonic Faraday-rotation fluctuations of radio waves when sounding the outer solar corona, *Astron. Lett.*, *26*(8), 544–552, doi:10.1134/1.1306991.

Efimov, A. I., L. A. Lukanina, A. I. Rogashkova, L. N. Samoznaev, I. V. Chashei, M. K. Bird, and M. Pätzold (2015a), Faraday-rotation fluctuations from radio-sounding measurements of the circumsolar plasma using polarized signals from the HELIOS-1 and HELIOS-2 space probes, *Astron. Rep.*, *59*(4), 313–326, doi:10.1134/S1063772915040022.

Efimov, A. I., L. A. Lukanina, A. I. Rogashkova, L. N. Samoznaev, I. V. Chashei, M. K. Bird, and M. Pätzold (2015b), Coronal radio occultation experiments with the Helios solar probes: correlation/spectral analysis of Faraday rotation fluctuations, *Sol. Phys.*, *290*, 2397–2408, doi:10.1007/s11207-015-0687-y.

Hamaker, J. P., and J. D. Bregman (1996), Understanding radio polarimetry. III. Interpreting the IAU/IEEE definitions of the Stokes parameters, *Astron. Astrophys. Suppl.*, *117*, 161–165.

Hollweg, J. V. (1974), Transverse Alfvén waves in the solar wind: Arbitrary **k**, **v**0, **B**0, and |δ**B**|, *J. Geophys. Res.*, *79*(10), 1539–1541, doi:10.1029/JA079i010p01539.

Hollweg, J. V. (2008), The solar wind: Our current understanding and how we got here, *J. Astrophys. Astron.*, *29*, 217–237, doi:10.1007/s12036-008-0028-8.

Hollweg, J. V., M. K. Bird, H. Volland, P. Edenhofer, C. T. Stelzried, and B. L. Seidel (1982), Possible evidence for coronal Alfvén waves, *J. Geophys. Res.*, *87*, 1–8, doi:10.1029/JA087iA01p00001.

Hollweg, J. V., S. R. Cranmer, and B. D. G. Chandran (2010), Coronal Faraday rotation fluctuations and a wave/turbulence-driven model of the solar wind, *Astrophys. J.*, *722*, 1495–1503, doi:10.1088/0004-637X/722/2/1495.

Imamura, T., et al. (2014), Outflow structure of the quiet Sun corona probed by spacecraft radio scintillations in strong scattering, *Astrophys. J.*, *788*, 117 (10pp), doi:10.1088/0004-637X/788/2/117.

Institute of Electrical and Electronics Engineers (1969), Standard definition of terms for radio wave propagation, *IEEE Trans.*, *AP-17*, 270–275.

Ingleby, L. D., S. R. Spangler, and C. A. Whiting (2007), Probing the large-scale structure of the solar corona with Faraday rotation measurements, *Astrophys. J.*, *668*, 520–532, doi:10.1086/521140.

Jensen, E. A. (2007), High frequency Faraday rotation observations of the solar corona, PhD thesis, Univ. of California, Los Angeles.

Jensen, E. A., and C. T. Rusell (2009), Coronal magnetic field analysis with Faraday rotation observations of Alfvén waves, *Geophys. Res. Lett.*, *36*, L05104, doi:10.1029/2008GL036257.

Jensen, E. A., M. M. Bisi, A. R. Heiles, C. Heiles, T. Minter, and F. Vilas (2013a), Measurements of Faraday rotation through the solar corona during the 2009 Solar Minimum with the MESSENGER spacecraft, *Sol. Phys.*, *285*, 83–95, doi:10.1007/s11207-012-0213-4.

Jensen, E. A., M. Nolan, M. M. Bisi, I. Chashei, and F. Vilas (2013b), MESSENGER observations of magnetohydrodynamic waves in the solar corona from Faraday rotation, *Sol. Phys.*, *285*, 71–82, doi:10.1007/s11207-012-0162-y.

Jensen, E. A., R. Frazin, C. Heiles, P. Lamy, A. Llebaria, J. D. Anderson, M. M. Bisi, and R. A. Fallows (2016), The comparison of total electron content between radio and Thompson scattering, *Sol. Phys.*, *291*, 465–485, doi:10.1007/s11207-015-0834-5.

Jensen, E. S., M. K. Bird, S. W. Asmar, L. Iess, J. D. Anderson, and C. T. Russell (2005), The Cassini solar Faraday rotation experiment, *Adv. Space Res.*, *36*, 1587–1594, doi:10.1016/j.asr.2005.09.039.

Jian, L. K., P. J. Macniece, A. Taktakishvilli, D. Odstrcil, B. Jackson, H. S. Yu, P. Riley, I. V. Sokolov, and R. M. Evans (2015), Validation for solar wind prediction at Earth: Comparison of coronal and heliospheric models installed at the CCMC, *Space Weather*, *13*, 316–338, doi:10.1002/2015SW001174.

Jones, S. I., and J. M. Davila (2009), Localized plasma density enhancements observed in STEREO COR1, *Astrophys. J.*, *701*, 1906–1910, doi:10.1088/0004-637X/701/2/1906.

Kooi, J. (2016), Very large array Faraday rotation studies of coronal plasma, PhD thesis, Univ. of Iowa.

Kooi, J. E., P. D. Fisher, J. J. Buffo, and S. R. Spangler (2014), Measurements of coronal Faraday rotation at 4.6 R☉, *Astrophys. J.*, *784*, 68 (17pp), doi:10.1088/0004-637X/784/1/68.

LeChat, G., J. C. Kasper, O. Cohen, and S. R. Spangler (2014), Diagnostics of the solar corona from comparison between Faraday rotation measurements and magnetohydrodynamic simulations, *Astrophys. J.*, *763*, 163 (7pp), doi:10.1088/0004-637X/789/2/163.

Mancuso, S., and M. V. Garzelli (2013), Radial profile of the inner heliospheric magnetic field as deduced from Faraday rotation observations, *Astron. Astrophys.*, *553*, A100, doi:10.1051/0004-6361/201220319.

Mancuso, S., and S. R. Spangler (1999), Coronal Faraday rotation observations: Measurements and limits on plasma inhomogeneities, *Astrophys. J.*, *525*, 195–208, doi:10.1086/307896.

Mancuso, S., and S. R. Spangler (2000), Faraday rotation and models for the plasma structure of the solar corona, *Astrophys. J.*, *480–491*, doi:10.1086/309205.

Mathioudakis, M., D. B. Jess, and R. Erdelyi (2013), Alfvén waves in the solar atmosphere. From theory to observations, *Space Sci. Rev.*, *175*, 1–27, doi:10.1007/s11214-012-9944-7.

McIntosh, S. W., B. De Pontieu, M. Carlsson, V. Hansteen, P. Boerner, and M. Goossens (2011), Alfvénic waves with sufficient energy to power the quiet solar corona and fast solar wind, *Nature*, *475*, 477–480, doi:10.1038/nature10235.

Mercier, C., and G. Chambe (2015), Electron density and temperature in the solar corona from multifrequency radio imaging, *Astron. Astrophys.*, *583*, A101, doi:10.1051/0004-6361/201425540.

Nakariakov, V. M., and E. Verwichte (2005), Coronal waves and oscillations, *Living Rev. Sol. Phys.*, *2*, doi:10.12942/lrsp-2005-3.

Oberoi, D., and C. J. Lonsdale (2012), Media responsible for Faraday Rotation: A review, *Radio Sci.*, *47*, RS0K08, doi:10.1029/2012RS004992.

Ofman, L. (2010), Wave modeling of the solar wind, *Living Rev. Sol. Phys.*, *7*, doi:10.12942/lrsp-2010-4.

Pätzold, M., M. K. Bird, H. Volland, G. S. Levy, B. L. Seidel, and C. T. Stelzried (1987), The mean coronal magnetic field determined from HELIOS Faraday rotation measurements, *Sol. Phys.*, *109*, 91–105, doi:10.1007/BF00167401.

Roberts, D. A. (2010), Demonstrations that the solar wind is not accelerated by waves or turbulence, *Astrophys. J.*, *711*, 1044–1050, doi:10.1088/0004-637X/711/2/1044.

Sakurai, T., and S. R. Spangler (1994), The study of coronal plasma structures and fluctuations with Faraday rotation measurements, *Astrophys. J.*, *434*, 773–785, doi:10.1086/174780.

Song, P., and C. T. Russell (1999), Time series data analyses in space physics, *Space Aci. Rev.*, *87*, 387–463, doi:10.1023/A:1005035800454.

Spangler, S. R. (2002), The amplitude of magnetohydrodynamic turbulence in the inner solar wind, *Astrophys. J.*, *576*, 997–1004, doi:10.1086/341889.

Spangler, S. R. and C. A. Whiting (2009), *Remote Sensing of the Corona and Solar Wind, IAU Symposium*, *IAU Symposium*, vol. 257, edited by N. Gopalswamy and D. F. Webb, Cambridge Univ. Press, Cambridge, U. K., doi:10.1017/S1743921309029834.

Spruit, H. C. (1981), Magnetic flux tubes, in *The Sun as a Star*, edited by S. Jordan, pp. 385–412, NASA SP-450, Paris/Washington, CNRS/NASA.

Srinivasan, D. K., M. E. Perry, K. B. Fielhauer, D. E. Smith, and M. T. Zuber (2007), The radio frequency subsystem and radio science on the MESSENGER mission, *Space Sci. Rev.*, *131*, 557–571, doi:10.1007/s11214-007-9270-7.

Stilwell, R. K., R. E. Wallis, and M. L. Edwards (2003), A circularly polarized, electrically scanned slotted waveguide array suitable for high temperature environments, Proceedings of the Institute of Electrical and Electronics Engineers International Symposium on Antennas and Propagation and United States National Committee/Canadian National Committee/International Union of Radio Science North American Radio Science Meeting, Columbus, OH, vol. 3, 1030–1033.

Timmer, J., and M. Köenig (1995), On generating power law noise, *Astron. Astrophys.*, *300*, 707–710.

Tomczyk, S., S. W. McIntosh, S. L. Keil, P. G. Judge, T. Schad, D. H. Seeley, and J. Edmondson (2007), Alfvén waves in the solar corona, *Science*, *317*, 1192–1196, doi:10.1126/science.1143304.

You, X. P., W. A. Coles, G. B. Hobbs, and R. N. Manchester (2012), Measurement of the electron density and magnetic field of the solar wind using millisecond pulsars, *Mon. Notices R. Astron. Soc.*, *422*, 1160–1165, doi:10.1111/j.1365-2966.2012.20688.x.